Probing strongly driven and strongly coupled superconducting qubit-resonator system

Oleh V. Ivakhnenko[1,2],[*] Christoforus Dimas Satrya[3],[†] Yu-Cheng Chang[3], Rishabh Upadhyay[3],
Joonas T. Peltonen[3], Sergey N. Shevchenko[1], Franco Nori[2,4], and Jukka P. Pekola[3]

[1] *B. Verkin Institute for Low Temperature Physics and Engineering, Kharkiv 61103, Ukraine*
[2] *Center for Quantum Computing, RIKEN, Wako, Saitama, 351-0198, Japan*
[3] *Pico group, QTF Centre of Excellence, Department of Applied Physics,*
Aalto University, P.O. Box 15100, FI-00076 Aalto, Finland and
[4] *Physics Department, The University of Michigan, Ann Arbor, MI 48109-1040, USA*
(Dated: August 6, 2025)

We investigated a strongly driven qubit strongly connected to a quantum resonator. The measured system was a superconducting flux qubit coupled to a coplanar-waveguide resonator which is weakly coupled to a probing feedline. This hybrid qubit-resonator system was driven by a magnetic flux and probed with a weak probe signal through the feedline. We observed and theoretically described the quantum interference effects, deviating from the usual single-qubit Landau-Zener-Stückelberg-Majorana interferometry, because the strong coupling distorts the qubit energy levels.

I. INTRODUCTION

Circuit quantum electrodynamics provides a platform for quantum phenomena experiments and quantum technology applications [1–7]. Natural microscopic quantum systems, when driven or coupled, experience this perturbation usually weakly [8]. In contrast, artificial quantum systems allow to realize both strong coupling and strong driving [9–11]. The layout when natural or artificial atoms are *strongly coupled* to cavities provides both new phenomena in quantum physics and is important for quantum engineering. Strong coupling [12–19] was recently studied for both natural and artificial atoms. In quantum computation, strong coupling increases the speed of gate operations and information exchange [20].

For the control of quantum systems *strong periodic driving* provides a convenient tool. Since theoretically this relates to the transitions between energy levels and their interference, this regime can be studied using Landau-Zener-Stückelberg-Majorana (LZSM) interferometry [19, 21–32].

Here we consider two important regimes of operation for quantum system: strong coupling and strong driving, both of which have attracted attention. However, these two aspects rarely meet and are realized in one device. Recently efforts in this direction were done in Ref. [20], which studied two strongly driven double quantum dots strongly coupled to a cavity.

In this work, we study a flux qubit strongly coupled to a resonator. We measure the transmission of the driven hybrid qubit-resonator system and observe quantum interference effects. We are able to reproduce the measured interference with our theoretical model. This system provides a useful framework for quantum thermodynamic experiments, for example for measuring heat produced by a driven qubit [33–36], and the realization of a quantum heat engine and refrigerator, where a driven qubit is coupled to two dissipative resonators [37, 38], and a heat engine/refrigerator cycles for a single qubit with modulated energy levels [39–41].

II. THE MEASURED SYSTEM AND DEVICE

A quantum resonator is coupled to a qubit, with a coupling g, as depicted in Fig. 1(a). The characteristic energy of the resonator is hf_R and the qubit energy is hf_Q that can be tuned by a magnetic flux Φ. The hybrid qubit-resonator system is driven by two signals. The first one is a probe tone with amplitude A_P and frequency f_P, which excites and probes the resonator. The second signal is a drive tone, with amplitude A_D and frequency f_D, which modulates cyclically the qubit energy.

The physical realization of this system is shown in Fig. 1(b). A quarter-wavelength ($\lambda/4$) coplanar waveguide (CPW) resonator is capacitively connected to a probing feedline. The fundamental-mode resonance of the resonator is f_{R1}, with the higher-mode resonances: $f_{R3} = 3f_{R1}$ and $f_{R5} = 5f_{R1}$.

Here we focus on the interaction between the qubit and the mode resonance f_{R3}, which we define as the resonance frequency f_0. The shorted end of the resonator is shunted galvanically by a flux qubit composed of a parallel inductor L and three Josephson junctions [42] where two of them are designed to be identical in size, shown by the scanning electron microscope (SEM) image in Fig. 1(c). The strength of the interaction between resonator and qubit can be controlled by the inductance L, $g \sim L$. The flux qubit Hamiltonian is

$$H_Q = -\frac{1}{2}\hbar(\Delta\sigma_x + \varepsilon\sigma_z), \qquad (1)$$

where $\hbar\varepsilon = 2I_p(\Phi - \Phi_0/2)$, I_p stands for the persistent current, Δ is the minimal qubit energy splitting, Φ_0 is the magnetic-flux quantum, and Φ is the external magnetic flux applied through the qubit loop. The qubit energy is

$$\omega_Q = 2\pi f_Q = \sqrt{\Delta^2 + \varepsilon^2}, \qquad (2)$$

---
[*] oleh.ivakhnenko@riken.jp; Contributed equally to this work
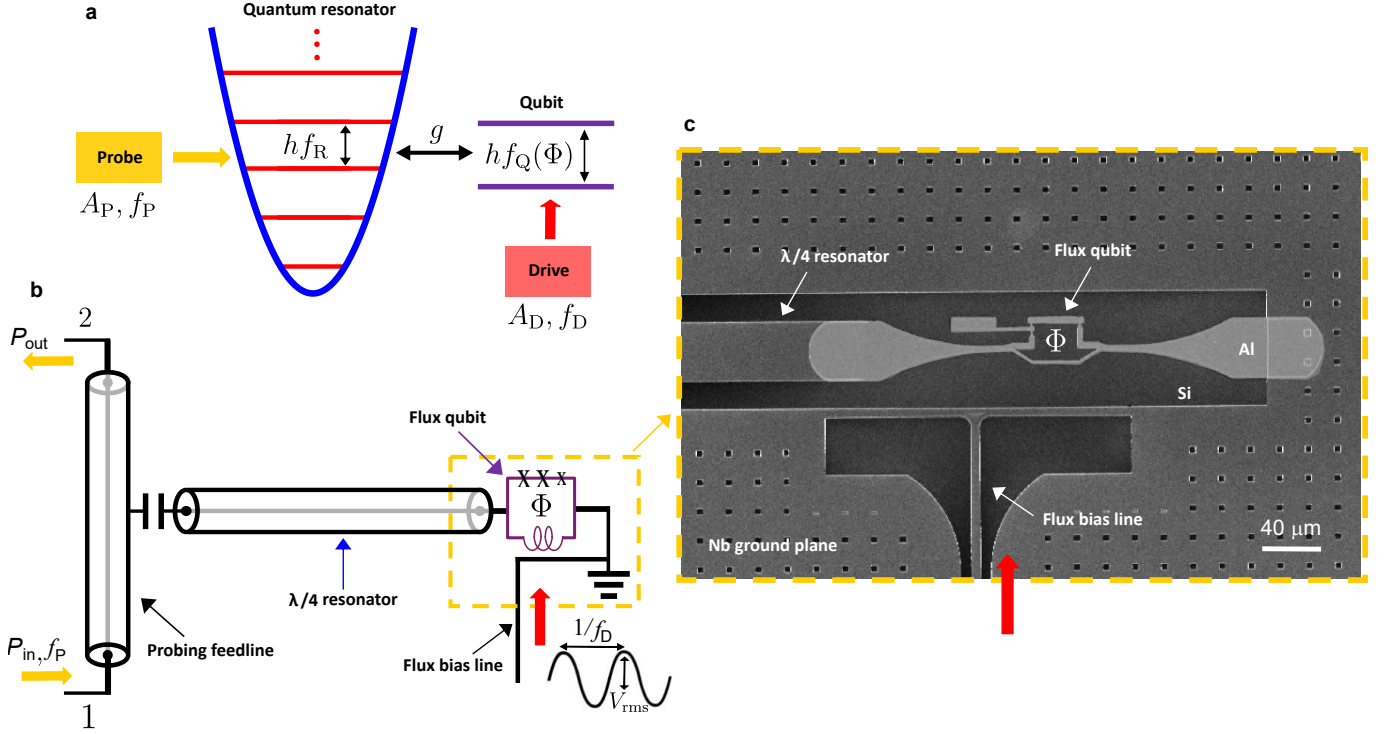[†] christoforus.satrya@aalto.fi; Contributed equally to this work

FIG. 1. **a**, A quantum resonator is coupled strongly to a qubit via g. The hybrid system is driven by two signals, probe and drive tones, with frequencies f_P and f_D, respectively, and their amplitudes A_P and A_D. **b**, The physical realization of the qubit-resonator device. A $\lambda/4$ resonator is capacitively coupled to a probing feedline and shorted by a flux qubit with three Josephson junctions in parallel with an inductor L [42]. **c**, Scanning electron microscope image of the fabricated device shows the resonator shunted by the flux qubit. The on-chip flux bias line is located nearby the qubit to inject the drive tone. The resonator and feedline are made of 200 nm-thick Nb film (bright gray) on top of AlO_x/Si substrate (dark gray), while the flux qubit is made of Al film (light grey). The transmission $|S_{21}|$ measurement is carried out through the feedline of Port-1 and Port-2. See Fig. 8 for the whole layout of the device.

where ε is tuned by applying the flux Φ through the loop. In the experiments, we can apply static (DC) and alternating (AC) fluxes to the qubit loop as

$$\Phi = \Phi_{DC} + \Phi_{AC} \sin(2\pi f_D t), \qquad (3)$$

where the second term originates from the drive tone. The DC flux (Φ_{DC}) is controlled by applying a DC current to the coil located outside the sample holder. The AC flux is controlled by the drive tone injected through an on-chip flux bias line inductively coupled to the qubit loop. The drive tone is generated by applying a sinusoidal voltage from a signal generator with voltage rms V_{rms} and frequency f_D.
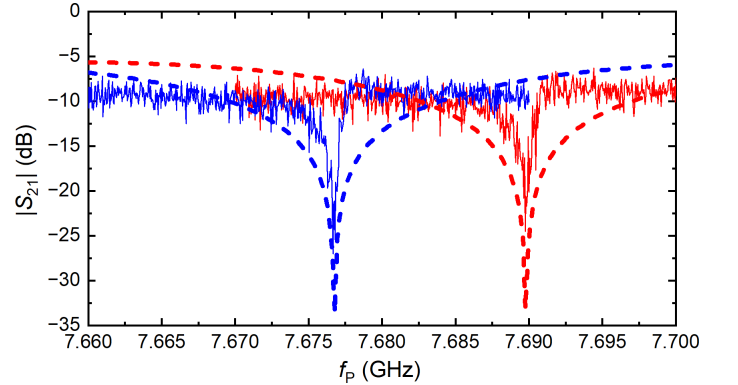

FIG. 2. Measured transmission $|S_{21}|$ (with $P_{in} = -40$ dBm and $A_D = 0$) is plotted using solid curves. The blue fluctuating curve is at a flux bias $\Phi_{DC}/\Phi_0 = 0$, with the resonator resonant frequency $f_0 = 7.6767$ GHz. The total photon relaxation rate, that defines the line-width is approximately equivalent to $\kappa/2\pi \sim 4.71$ MHz. The red fluctuating curve is at a flux bias $\Phi_{DC}/\Phi_0 = 0.5$, with resonant frequency of the qubit-resonator system at $f_{QR} = 7.6898$ GHz. Thus, the dispersive shift is $\chi = 13.1$ MHz. The dashed curves are the theoretical transmissions, numerically calculated from the Lindblad equation with Hamiltonian (7) and transmission coefficient (6).

A probe signal with power P_{in} and frequency f_{P} is applied through Port-1 of the feedline, and the output signal coming out from Port-2 of the feedline is measured. With a vector network analyzer (VNA), the scattering parameter (transmission), whose amplitude is

$$|S_{21}(f)| = \sqrt{P_{\mathrm{out}}(f)/P_{\mathrm{in}}(f)}, \qquad (4)$$

can be measured. The power P_{in} determines the probe amplitude A_{P}. The detailed measurement setup and fabrication of the device are described in Appendices B and C.

III. THEORETICAL DESCRIPTION

A. Hamiltonian

Here we describe the system theoretically with numerical simulation of the modified Jaynes–Cummings Hamiltonian to investigate probing and driving of the qubit-resonator system. First, we write the Hamiltonian of the flux qubit-resonator system in the diabatic basis [40, 43, 44],

$$H_{\mathrm{tot}} = H_{\mathrm{Q}} + H_{\mathrm{R}} + H_{\mathrm{C}} + H_{\mathrm{P}} + H_{\mathrm{D}}, \qquad (5a)$$

$$H_{\mathrm{Q}} = \hbar \left(-\frac{\Delta}{2}\sigma_x - \frac{\varepsilon_0}{2}\sigma_z \right), \qquad (5b)$$

$$H_{\mathrm{R}} = \hbar\omega_{\mathrm{r1}} \left(a^\dagger a + \frac{1}{2} \right), \qquad (5c)$$

$$H_{\mathrm{C}} = -\hbar g \left(a + a^\dagger \right) \sigma_z, \qquad (5d)$$

$$H_{\mathrm{P}} = \hbar A_{\mathrm{P}} \left(a e^{i\omega_{\mathrm{P}}t} + a^\dagger e^{-i\omega_{\mathrm{P}}t} \right), \qquad (5e)$$

$$H_{\mathrm{D}} = -\hbar \frac{A_{\mathrm{D}}\sin\omega_{\mathrm{D}}t}{2}\sigma_z, \qquad (5f)$$

where H_{tot} is the total Hamiltonian of the system, H_{Q} is the qubit Hamiltonian, with Δ being the minimal energy gap, ε_0 is constant detuning, and $\sigma_{x,y,z}$ are Pauli matrices. Moreover, H_{R} is the resonator Hamiltonian, where a and $a^\dagger$ are the annihilation and creation operators for the resonator, and $\omega_{\mathrm{r1}} = 2\pi f_0$ is the resonator frequency, which interacts with the qubit. H_{C} is the coupling Hamiltonian, where g is qubit-resonator coupling strength. H_{P} is the probe signal Hamiltonian, where the probe frequency for the interferometry is $\omega_{\mathrm{P}} \approx \omega_{\mathrm{r1}}$ and the probe amplitude is A_{P}. H_{D} is the qubit driving Hamiltonian, where A_{D} is the driving amplitude, and $f_{\mathrm{D}} = \omega_{\mathrm{D}}/2\pi$ is the driving frequency.

To study theoretically the transmission coefficient of the transmission line, we consider the absolute value of the imaginary part of the photon annihilation operator in the resonator [43]

$$\langle |\mathrm{Im}(a)| \rangle = \mathrm{Tr}(|\mathrm{Im}(a)|\rho) = |S_{21}|, \qquad (6)$$

where ρ is the density matrix of the qubit-resonator system. In the limit of a weak probe signal, we can take into account only the first two-photon states in the resonator. After applying the rotating-wave approximation (RWA) and transfer to the instantaneous eigenstate basis, we obtain the dressed Hamiltonian in RWA

$$H_{\mathrm{RWA}} = \hbar \left[\frac{1}{2}\delta\omega_{\mathrm{Q}}\sigma_z + \delta\omega_{r1}a^\dagger a \right. \qquad (7)$$

$$\left. +g\frac{\Delta}{\omega_{\mathrm{Q}}} \left(\sigma_+ a + \sigma_- a^\dagger \right) + A_{\mathrm{P}} \left(a + a^\dagger \right) \right],$$

where

$$\delta\omega_{\mathrm{Q}} = \omega_{\mathrm{Q}} - \omega_{\mathrm{P}}, \qquad (8a)$$

$$\omega_{\mathrm{Q}} = \sqrt{\Delta^2 + \varepsilon(t)^2}, \qquad (8b)$$

$$\delta\omega_{r1} = \omega_{r1} - \omega_{\mathrm{P}}, \qquad (8c)$$

$$\delta\omega_{\mathrm{D}} = \omega_{\mathrm{D}} - \omega_{\mathrm{P}}. \qquad (8d)$$

Here ω_{Q} is the instant qubit energy, as in Eq. (2). We now use this dressed RWA Hamiltonian to describe the theoretical spectroscopy of our qubit-resonator system for both the wide and narrow ranges of the probing frequency ω_{P} in Fig. 3 and interferometry in Fig. 4. We use the Hamiltonian of Eq. (7) in the Lindblad equation (A3) with Lindblad operators (A1a) for the numerical calculations, more details of the theoretical description and transfer between bases and dressed states are presented in Appendix A. To numerically simulate this system, we solved the Lindblad master equation using the QuTiP library [45–47].

IV. RESULTS AND DISCUSSION

The transmission (S_{21}) and spectroscopy of the device are presented in Fig. 2 and Fig. 3, where the system is driven only by the probe tone through the resonator while the drive tone from the flux-bias line is off. The transmission of the experimental data is subtracted to reach the same level of background as in the simulation. Transmission at $\Phi_{\mathrm{DC}}/\Phi_0 = 0$, where the resonator is

TABLE I. Parameters used for the simulations

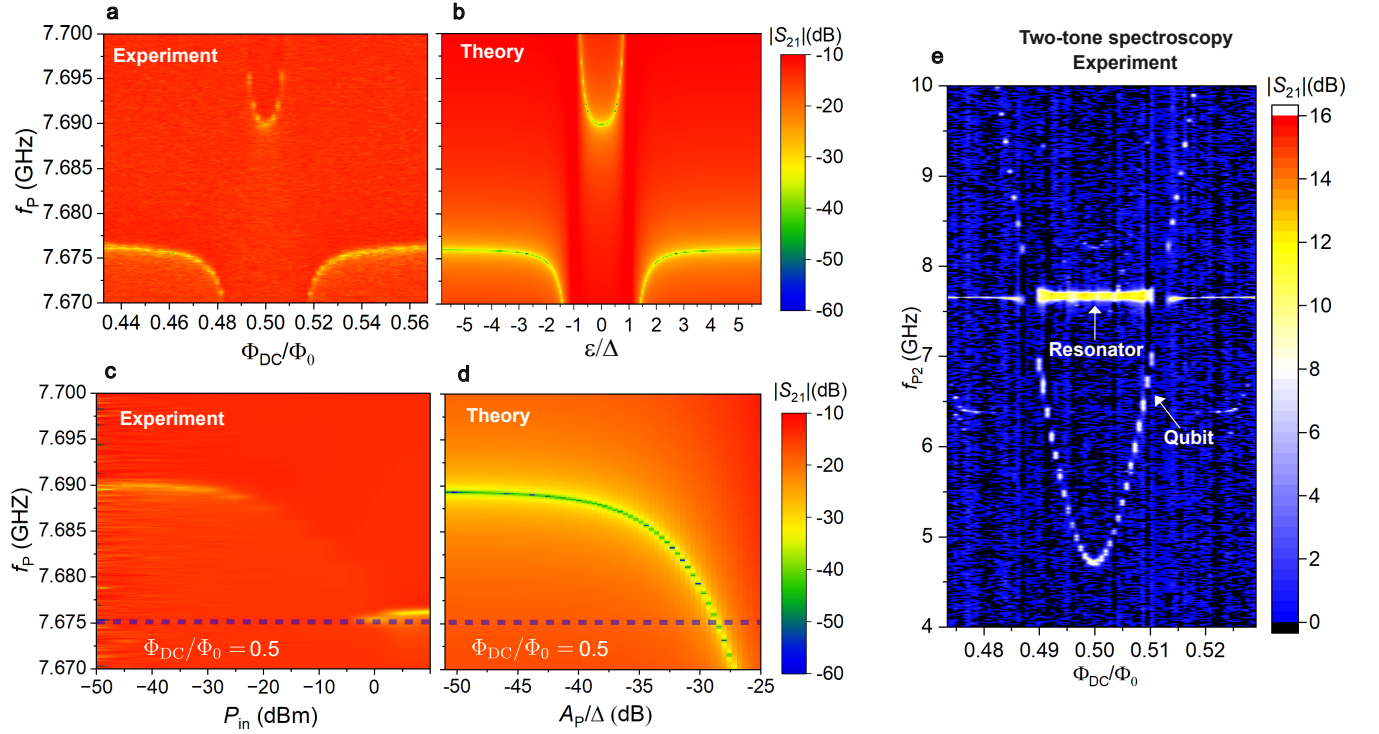| Quantity	Symbol	Value
Minimum qubit frequency	$\Delta/2\pi$	5.41 GHz
Resonator first-mode frequency	$f_0/2\pi$	7.6767 GHz
Qubit-resonator coupling	$g/2\pi$	177 MHz
Number of photons in resonator	N	2
Relaxation rate	$\Gamma_1/2\pi$	3 MHz
Dephasing rate	$\Gamma_2/2\pi$	1.5 MHz
Resonator relaxation rate	$\kappa/2\pi$	4.71 MHz
Probe amplitude	$A_{\mathrm{P}}/2\pi$	1 MHz

FIG. 3. Spectroscopy of the qubit-resonator system. Here the system is driven only by the probe tone through the resonator from the feedline with $P_{\text{in}} = -40$ dBm. The qubit drive from the flux-bias line is off, $A_{\text{D}} = 0$. One-tone spectrosopy: **a**, experiment and **b**, theory. **c-d**, Spectroscopy at fixed flux bias $\Phi_{\text{DC}}/\Phi_0 = 0.5$ with varying probe amplitude: **c**, experiment and **d**, theory. The horizontal dashed purple lines indicate the resonance frequency of the resonator f_0. **e**, Two-tone spectroscopy experiment showing the interaction of the qubit and resonator energy levels.

fully decoupled from the qubit, shows the resonance of the resonator f_0, shown in Fig. 2. At $\Phi_{\text{DC}}/\Phi_0 = 0.5$ the measured resonance is pushed toward higher frequency due to dispersive interaction with the qubit. Sweeping the Φ_{DC}/Φ_0 towards 0.5 shifts the measured resonance frequency f_{QR}, due to the hybridization of the resonator and qubit.

When the qubit energy is in resonance with f_0, the Rabi splitting is observed, as shown in Fig. 3(a). The coupling g is observed to be around 177 MHz. We calculate the transmission theoretically, and by adjusting the parameters g and Δ we achieve good agreement between theory and the experiment, as shown in Fig. 3(b).

We also fix the flux bias at $\Phi_{\text{DC}}/\Phi_0 = 0.5$ and sweep the power P_{in}. At higher P_{in}, the qubit is overpopulated by the probe tone; thus the resonance shifts and reaches back to the frequency f_0 as shown in Fig. 3(c), which we can reproduce theoretically in Fig. 3(d). The purple dashed line shows the resonance line f_0.

Moreover, a two-tone spectroscopy is performed to measure the qubit transitions and their interaction with the resonator as shown in Fig. 3(e). The second probe tone with frequency $f_{\text{P,2}}$ is applied through the feedline to excite the system. When $f_{\text{P,2}}$ is in resonance with the frequency of the dressed qubit state which is very close to qubit frequency at the large detuning, the S_{21} signal of the first probe changes. It shows that the qubit energy

folows the parabola of Eq. (2) and crosses the resonator energy at frequency ~ 7.6767 GHz. The presented two-tone spectroscopy data here is measured from the sister sample, where it is observed $\Delta \sim 4.9$ GHz.

Furthermore, the system is also driven by both the probe and drive signals. The probe frequency f_{P} is fixed at f_0 and the drive frequency f_{D} at either 500 MHz or 1500 MHz. The transmission coefficient S_{21} is measured for varying V_{rms} and sweeping Φ_{DC}/Φ_0 around 0.5. We apply, with a weak power, $P_{\text{in}} = -40$ dBm to probe the system. The results of the interferometry for a two different driving frequencies $f_{\text{D}} = 500$ MHz and $f_{\text{D}} = 1500$ MHz shown in Fig. 4. The calculated upper qubit population is shown in Fig. 4(c,f). From these interferograms, we can see that the resonance lines density is the same for the transmission and qubit level occupation, but the shape of the resonances is different due to qubit-resonator quantum coupling. Moreover, we fix the flux bias at $\Phi_{\text{DC}}/\Phi_0 = 0.5$ and sweep the probe frequency f_{P} and drive amplitude A_{D}. The results of the interferometry are shown in Fig. 5 (experiments and simulations) with several different drive frequencies f_{D} shows similar behaviour in experiment and theory. The parameters used in the simulations are summarized in Table I. The parameters f_0, g and κ are obtained from the measurements, while the other parameters are adjusted to get the best match between experiments and simulations.
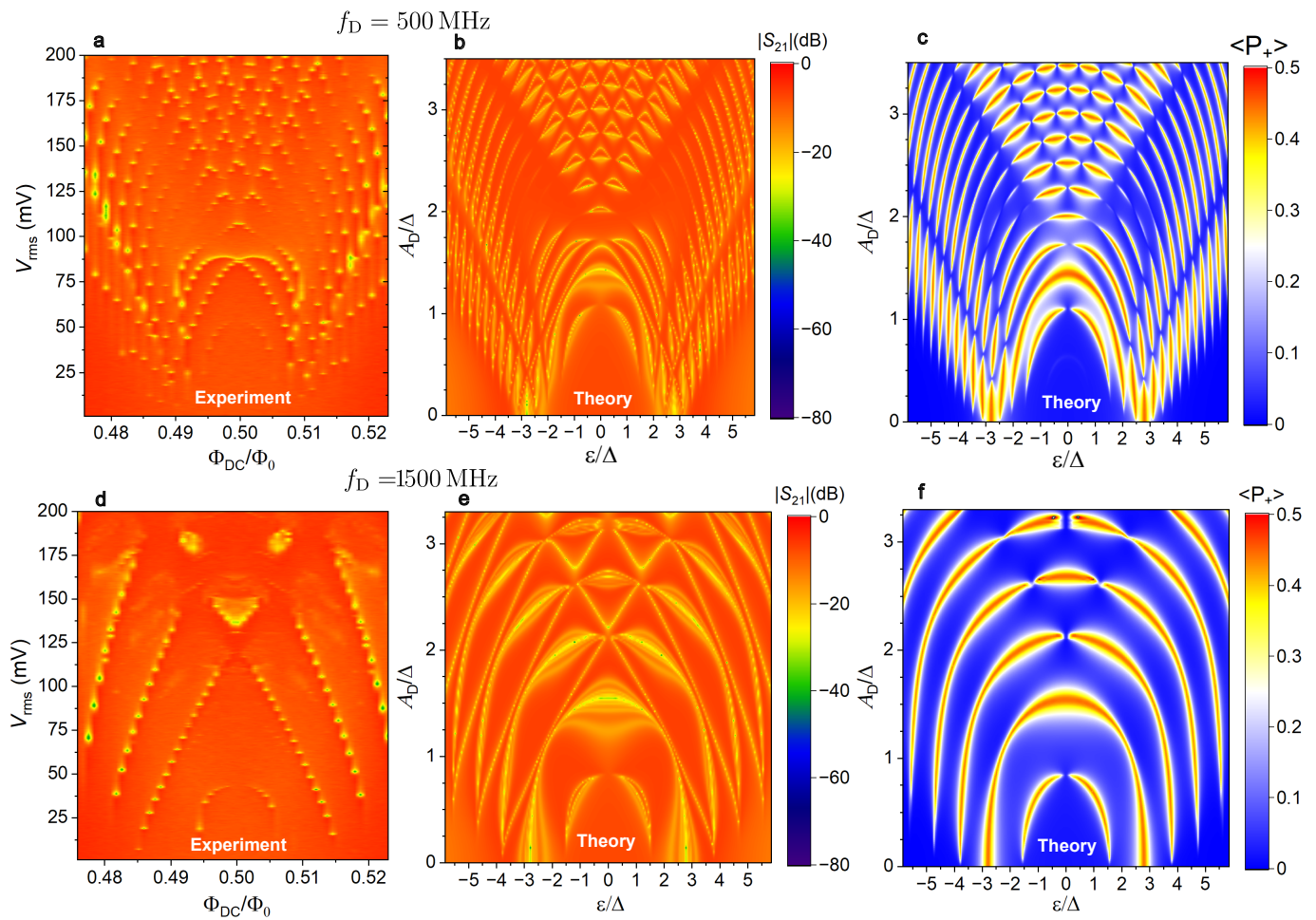
FIG. 4. Interferometry of the driven qubit-resonator system with fixed power $P_{in} = -40$ dBm and driving frequency $f_D = 500$ MHz for the upper panels and $f_D = 1500$ MHz for the lower ones. The probe frequency f_P is fixed at the resonance frequency f_0, and the drive amplitude is varied. Transmission: **a,d**, experiment and **b,e**, theory. **c,f**, The upper qubit population.

V. CONCLUSIONS

We measured and calculated the transmission of a strongly driven coupled resonator-flux qubit system. We observed quantum interference effects, different from the usual Landau-Zener-Stückelberg-Majorana interferometry due to strong coupling between the qubit and the resonator. The main difference from the usual multiphoton LZSM interference appears at low driving field amplitudes, where the impact of the strong coupling is more significant than the impact of driving. The instant adiabatic basis, which takes into account the driving to the eigenstate basis transfer, is well suited for this problem and gives good agreement with the experiment. The spectroscopy of the qubit is used for precisely calibrating the theoretical parameters of the system. When increasing the coupling strength, the distortions of the resonances become more pronounced. Our theory work here can be used to describe the behavior of a qubit strongly coupled to a quantum resonator, which could be used as a basis for a quantum heat engine and refrigerator in this regime where the resonator is more strongly coupled to the qubit than to the environment.
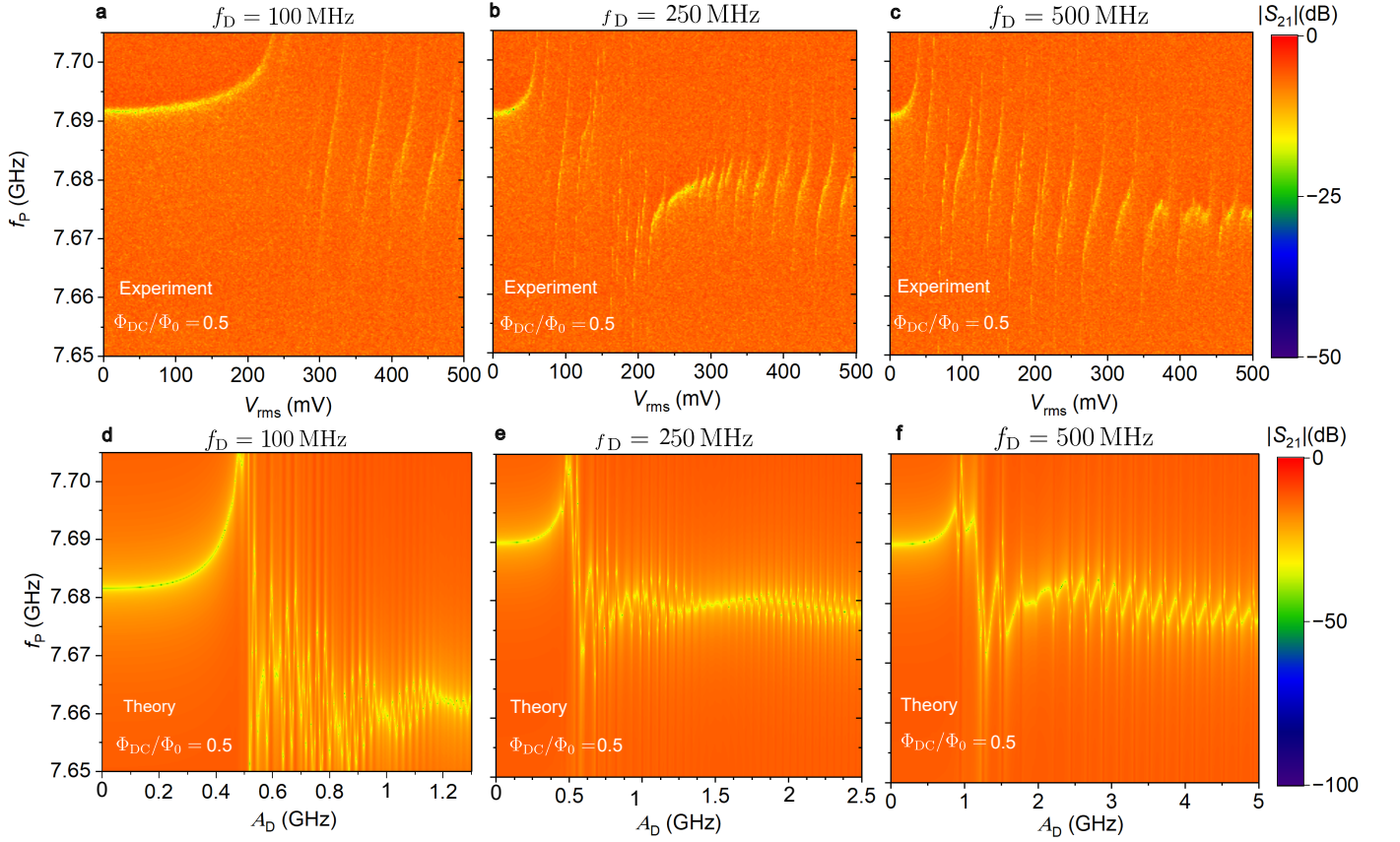
FIG. 5. Interferometry of the driven qubit-resonator system with fixed power $P_{in} = -40$ dBm and at fixed flux bias $\Phi_{DC}/\Phi_0 = 0.5$. The probe frequency f_P and drive amplitude A_D are varied. **(a-c)** are the measurement results at different drive frequency f_D, and **(d-f)** are the simulation results.

Appendix A: Detailed theoretical description

1. Dissipative environment

We use the Lindblad equation with initial Hamiltonian (5a) to which we add relaxation and dephasing for the qubit and relaxation for photon states in the resonator

$$L_1^D = \sigma_- \sqrt{\Gamma_1}, \qquad (A1a)$$
$$L_2^D = \sigma_z \sqrt{\Gamma_2}, \qquad (A1b)$$
$$L_3^D = a\sqrt{\kappa}, \qquad (A1c)$$

where $\Gamma_{1,2}$ are the relaxation and dephasing rates, and κ is the photon decay rate in resonator.

2. Instant eigenstate basis

To solve the Lindblad equation (A3) in the adiabatic (instantaneous eigenstate) basis, we need to transfer our Hamiltonian from the diabatic basis to the adiabatic (instant eigenstate) basis [48]. For this we use the static transfer matrix between bases

$$S = S^\dagger = \begin{pmatrix} \gamma_+ & \gamma_- \\ \gamma_- & -\gamma_+ \end{pmatrix}, \qquad (A2a)$$

$$H'_Q = SHS^\dagger = \hbar\frac{\omega_Q}{2}\sigma_z = \frac{1}{2}\begin{pmatrix} \omega_Q & 0 \\ 0 & -\omega_Q \end{pmatrix}, (A2b)$$

where $\gamma_\pm = \frac{1}{\sqrt{2}}\sqrt{1 \pm \frac{\varepsilon(t)}{\omega_Q}}$, and $\omega_Q = \sqrt{\Delta^2 + \varepsilon^2(t)}$ is the instant qubit angular frequency.

Then we solve numerically the Lindblad equation

$$\dot{\rho}(t) = -\frac{i}{\hbar}[H_{tot}, \rho] + \qquad (A3)$$

$$+\frac{1}{2}\sum_{i=1}^{3}\left[2L_i^D\rho(t)L_i^{D\dagger} - \rho(t)L_i^{D\dagger}L_i^D - L_i^{D\dagger}L_i^D\rho(t)\right],$$
$$(A4)$$

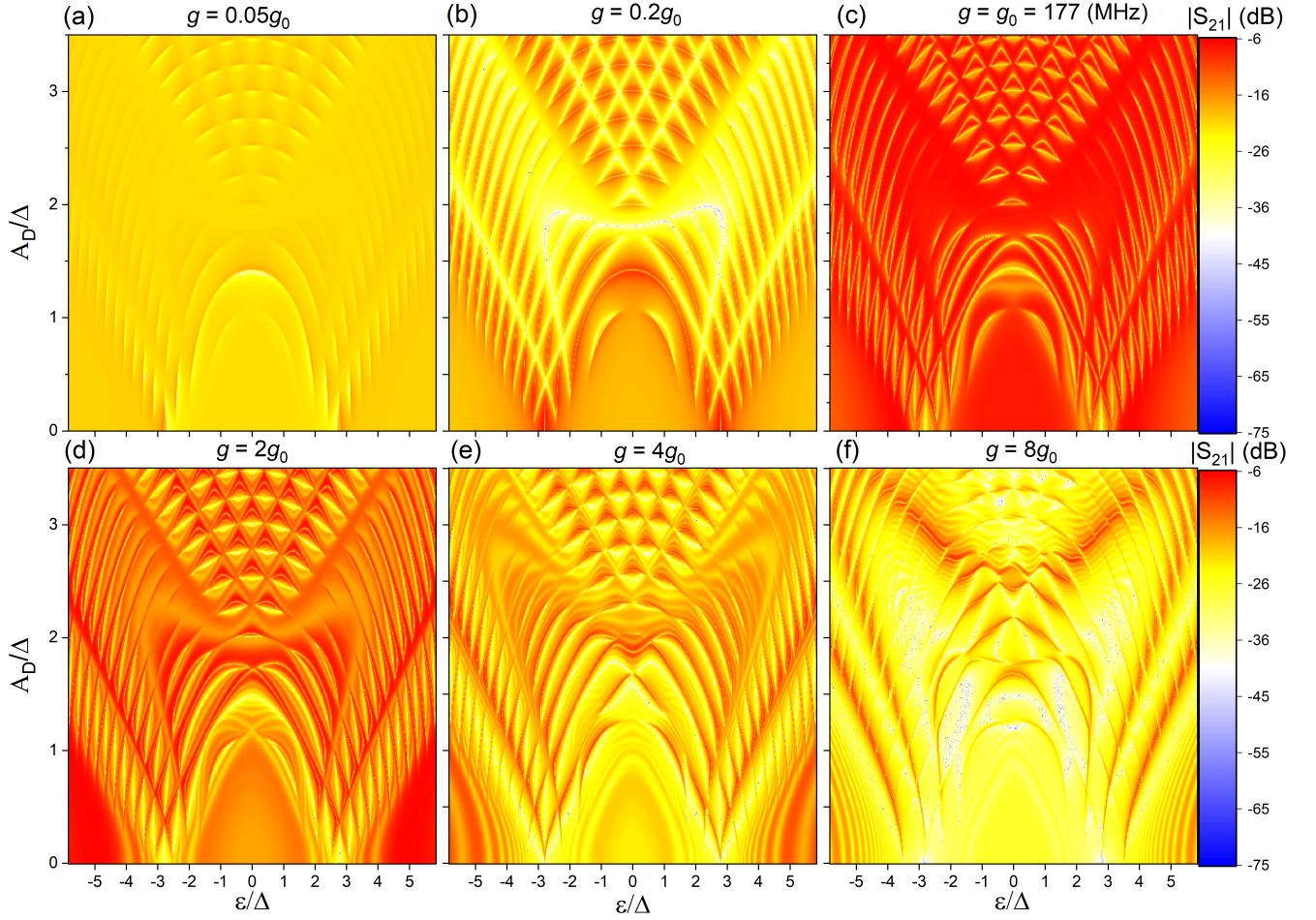where ρ is the density matrix. The theoretical spectro-

FIG. 6. Theoretical interferometry of the driven qubit-resonator system with fixed probing amplitude $A_P = 1$ MHz and driving frequency $\omega_D/2\pi = 500$ MHz, for different strengths of the qubit-resonator coupling g, where $g_0 = 177$ MHz was obtained from the spectroscopic calibration between theory and experiment shown in Fig. 3(a,b). The theoretical transmission coefficient $|S_{21}|$ is proportional to the averaged absolute value of imaginary part of the annihilation operator $|\text{Im}(<a>)|$.

scopic and interferometric results were obtained using the QuTiP [45–47] library.

Consider now qubit-resonator and qubit driving Hamiltonian in the instant eigenstate basis as

$$H'_C = -\hbar g \left(a^\dagger + a\right) \left(\frac{\varepsilon_0}{\omega_Q}\sigma_z - \frac{\Delta}{\omega_Q}\sigma_x\right). \quad \text{(A5)}$$

Using the lowering and raising operators for a qubit,

$$\sigma = \sigma_+ = \frac{1}{2}(\sigma_x + i\sigma_y), \quad \text{(A6a)}$$

$$\sigma^\dagger = \sigma_- = \frac{1}{2}(\sigma_x - i\sigma_y), \quad \text{(A6b)}$$

that allow us to simplify the interaction and driving operators, we obtain

$$H'_C = \hbar \left[g\frac{\Delta}{\omega_Q}(a^\dagger\sigma + a\sigma^\dagger) + g\frac{\Delta}{\omega_Q}(a\sigma + a^\dagger\sigma^\dagger) - \quad \text{(A7)} \right.$$

$$\left. -g\frac{\varepsilon_0}{\omega_Q}(a^\dagger + a)\sigma_z \right] \approx \hbar g\frac{\Delta}{\omega_Q}(a^\dagger\sigma + a\sigma^\dagger).$$

Here $g\frac{\Delta}{\omega_Q}(a\sigma + a^\dagger\sigma^\dagger)$ and $-g\frac{\varepsilon_0}{\omega_Q}(a^\dagger + a)\sigma_z$ can be neglected in the RWA, because they do not conserve the number of excitations in the system.

Then we can show the diagonalized Hamiltonian for a qubit-resonator system, known as the Jaynes-Cummings Hamiltonian, without driving and probing signals

$$H' = H_{JC} + H'_D + H_P, \quad \text{(A8a)}$$

$$H_{JC} = H'_Q + H_R + H'_C, \quad \text{(A8b)}$$

$$H'_Q = \hbar \frac{1}{2}\omega_Q\sigma_z, \quad \text{(A8c)}$$

$$H_R = \hbar\omega_r \left(a^\dagger a + \frac{1}{2}\right), \quad \text{(A8d)}$$

$$H'_C = \hbar g \left(\sigma_+ a + \sigma_- a^\dagger\right). \quad \text{(A8e)}$$

This diagonalized Hamiltonian is defined in the same basis as the relaxation and dephasing Lindblad operators.
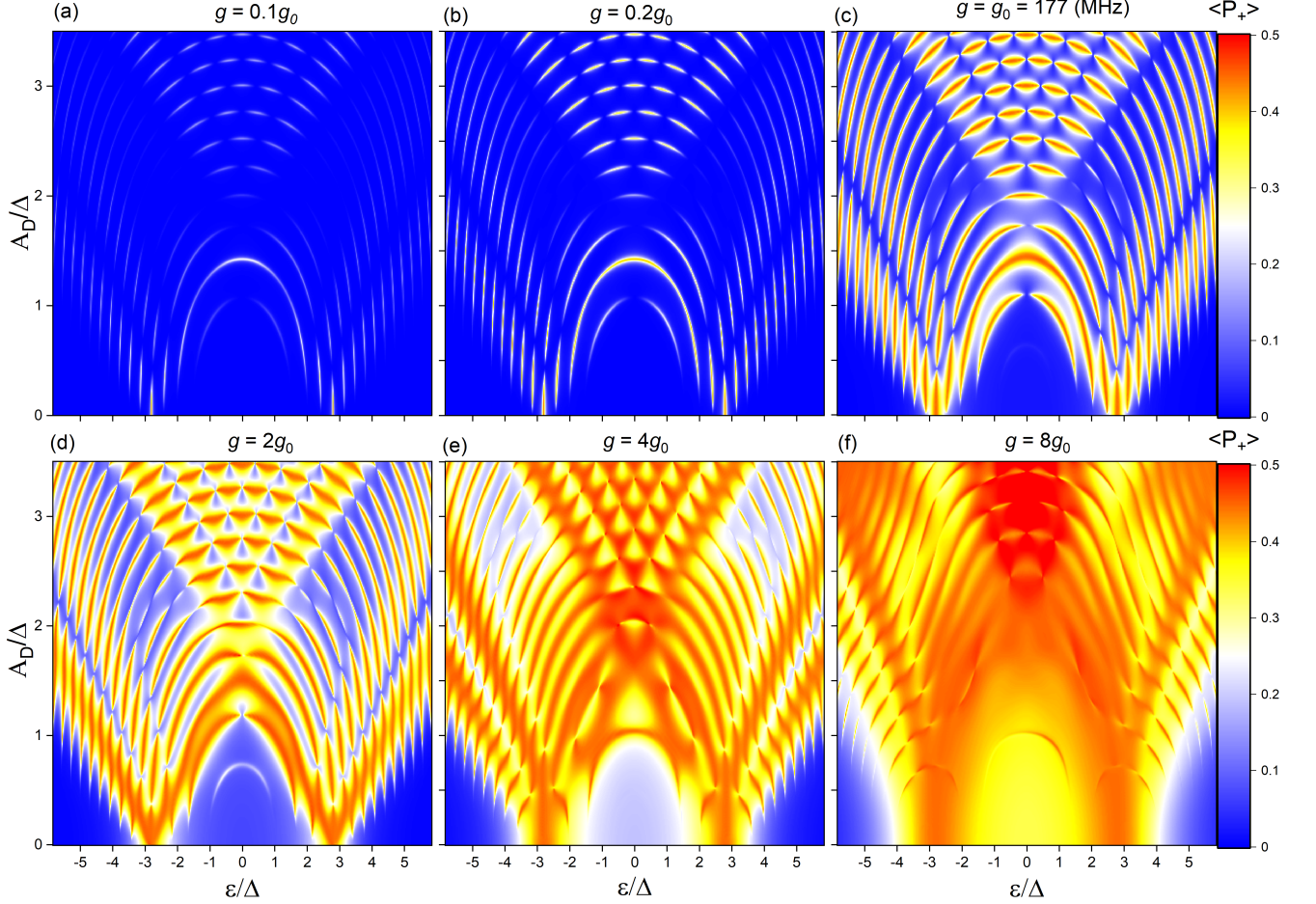
FIG. 7. Theoretical interferometry of the driven qubit-resonator system with fixed probing amplitude $A_P = 1$ MHz and driving frequency $\omega_D/2\pi = 500$ MHz, for different strengths of the qubit-resonator coupling g. For the upper level qubit occupation P_+ in the linear scale. Here $g_0 = 177$ MHz was obtained from the spectroscopy calibration between theory and experiment, as shown in Fig. 3(a,b).

3. Rotating wave approximation, dressed Hamiltonian

Here we describe a procedure of dressing the Hamiltonian. The dressing technique is convenient to describe systems with two driving signals with significantly different frequencies, like the ones studied here, with probing and driving signals, and it helps to eliminate the fast-rotating terms, which can provide an option to obtain an easier solution for two-tone interferometry [43, 49–51].

Consider our diagonalized Hamiltonian Eq. (A8a) of the driven system in the rotated basis [43]

$$H_{\mathrm{RWA}} = U H'_{\mathrm{tot}} U^\dagger + i\hbar \dot{U} U^\dagger, \qquad (A9)$$

with the rotating frame with probing frequency $\omega_P/2\pi$ as

$$U = \exp\left[i\omega_P t \left(a^\dagger a + \frac{\sigma_z}{2}\right)\right], \qquad (A10)$$

we then obtain the dressed Hamiltonian in the RWA (7).

4. Impact of the coupling strength

We show how the value of the coupling strength impacts the theoretical interferometry for the transmission coefficient in Fig. 6 and the qubit upper-level occupation probability in Fig. 7. As we expected, with growing coupling strength, the distortion of the resonances becomes stronger and spreads to higher driving amplitudes. For small coupling the interferometry pattern is very similar to the usual LZSM interferometry [24, 25, 27, 52]. When we increase the coupling to $g = 8g_0$ we notice large distortion in resonances, but these calculations may not be fully exact since we neglect counterrotating terms in the coupling in Eq. (A8) and come close to the range of the ultrastrong coupling, where they indeed should be included [12, 16].
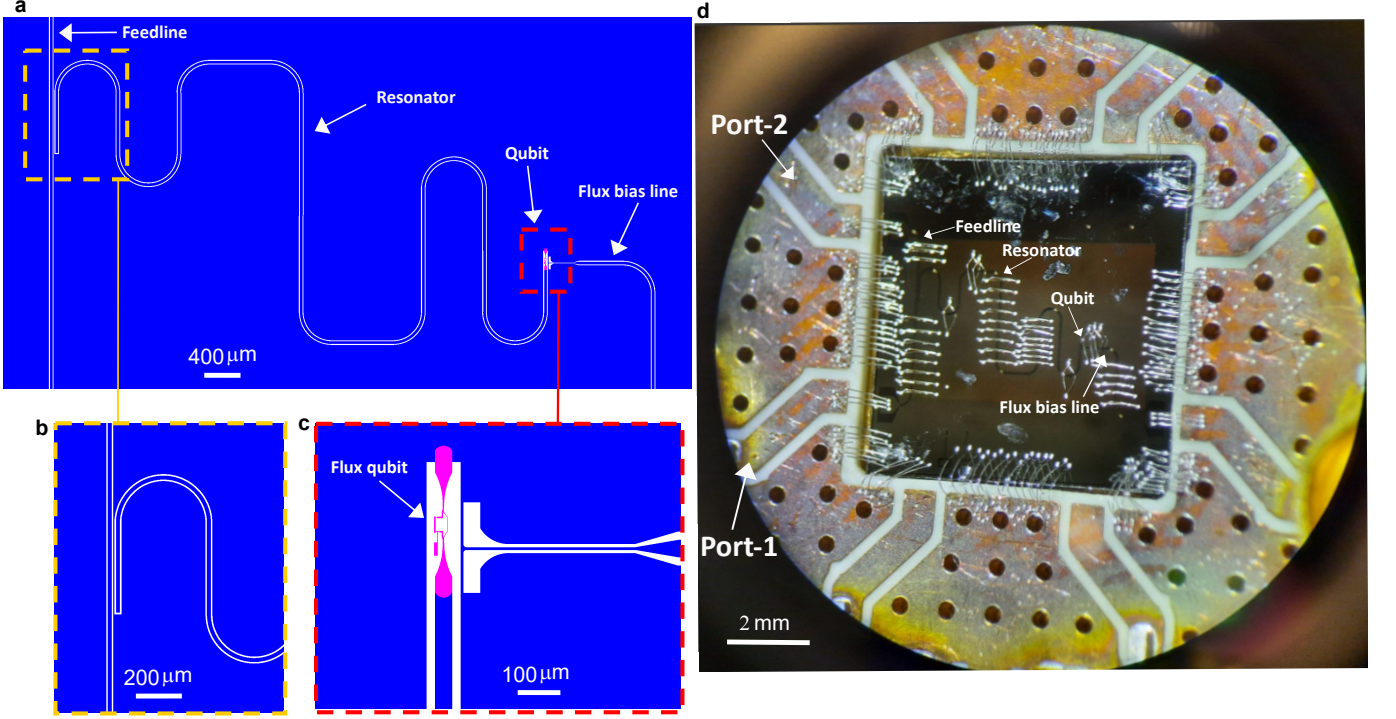
FIG. 8. **a**, Layout of the fabricated device. The resonator is capacitevely coupled to the nearby feedline. The flux qubit shunts the other side of the resonator with a nearby flux bias line to drive the qubit. The blue background color represents the Nb film and the purple color represents the Al film. **b**, The feedline coupled to the resonator. **c**, The flux qubit coupled to the nearby flux bias line. **d**, The fabricated device with size 7mm x 7mm on top of the holder. The transmission $|S_{21}|$ measurement is carried out through the feedline of Port-1 and Port-2, shown on the left side of the disk.

Appendix B: Fabrication methods

The fabrication of the device is done in a several processes on a 675 μm-thick and highly resistive silicon (Si) substrate, resulting in the device shown in Fig. 1(a-c). The fabrication consists of two main steps: (1) fabricating niobium (Nb) structures (resonator, feedline, ground plane, and pads), and (2) fabricating flux qubit made of three junctions of superconductor–insulator–superconductor (SIS) with aluminium (Al) film. A 40 nm-thick AlO_x layer is deposited onto a silicon substrate using atomic layer deposition, followed by a deposition of a 200 nm-thick Nb film using DC magnetron sputtering. A positive electron beam resist, AR-P6200.13, is spin-coated with a speed of 6000 rpm for 60 s, and is post-baked for 9 minutes at 160°C, which is then patterned by electron beam lithography (EBL) and etched by reactive ion etching. A shadow mask defined by EBL on a 1 μm-thick poly(methyl-metacrylate)/copolymer resist bilayer is used to fabricate the flux qubit made of an Al film connecting the resonator to the ground plane [42]. Before the deposition of the Al film, the Nb surface is cleaned in-situ by Ar ion plasma milling for 60 s. At the final stage, after liftoff in hot acetone (52 degrees for 30 minutes) and cleaning with isopropyl alcohol, the substrate is diced by an automatic dicing-saw machine to the size of 7mm x 7mm and wire-bonded to a copper holder for the low-temperature characterization. The layout of the device and the fabricated sample are shown in Fig. 8.

Appendix C: Experimental setup

Measurements are performed in a Bluefors cryogen-free dilution refrigerator with a base temperature 30 mK. Using a vector network analyzer (VNA), a probe microwave tone is supplied to the feedline through a 90 dB of attenuation distributed at various temperature stages of the cryostat. The probe signal is then passed through two cryogenic circulators, before being amplified first by a 40 dB cryogenic HEMT amplifier, and secondly by a 40 dB room-temperature amplifier. The dc flux bias is supplied by a nearby superconducting coil connected to an isolated voltage source at room temperature. The drive tone is generated from a microwave generator in the VNA to the on-chip flux bias line through 40 dB attenuation. The device is sealed in a copper holder and covered by an Al shield. The measurement setup is shown in Fig. 9.
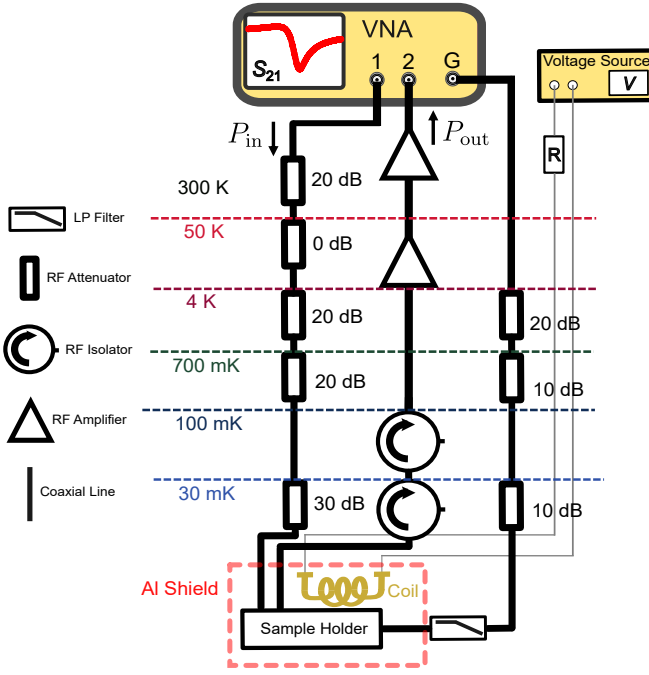
FIG. 9. Schematic of the experimental setup used in the measurements. Input power is injected through a series of cryogenic attenuators, and the output signal from the sample is amplified through cryogenic and room-temperature amplifiers to obtain $|S_{21}|$. The DC flux point Φ_{DC} is controlled by a superconducting coil that is current-biased through twisted pair. The AC flux is generated from a microwave generator in the VNA to the on-chip flux bias line.

[1] Z.-L. Xiang, S. Ashhab, J. Q. You, and F. Nori, Hybrid quantum circuits: Superconducting circuits interacting with other quantum systems, Rev. Mod. Phys. **85**, 623 (2013).

[2] X. Gu, A. F. Kockum, A. Miranowicz, Y.-x. Liu, and F. Nori, Microwave photonics with superconducting quantum circuits, Phys. Rep. **718–719**, 1 (2017).

[3] P. Krantz, M. Kjaergaard, F. Yan, T. P. Orlando, S. Gustavsson, and W. D. Oliver, A quantum engineer's guide to superconducting qubits, Appl. Phys. Rev. **6**, 021318 (2019).

[4] M. Kjaergaard, M. E. Schwartz, J. Braumüller, P. Krantz, J. I.-J. Wang, S. Gustavsson, and W. D. Oliver, Superconducting qubits: Current state of play, Annu. Rev. Conden. Matt. Phys. **11**, 369 (2020).

[5] A. A. Clerk, K. W. Lehnert, P. Bertet, J. R. Petta, and Y. Nakamura, Hybrid quantum systems with circuit quantum electrodynamics, Nat. Phys. **16**, 257 (2020).

[6] I. Carusotto, A. A. Houck, A. J. Kollár, P. Roushan, D. I. Schuster, and J. Simon, Photonic materials in circuit quantum electrodynamics, Nat. Phys. **16**, 268 (2020).

[7] A. Blais, A. L. Grimsmo, S. M. Girvin, and A. Wallraff, Circuit quantum electrodynamics, Rev. Mod. Phys. **93**,

025005 (2021).

[8] M. V. Gustafsson, T. Aref, A. F. Kockum, M. K. Ekström, G. Johansson, and P. Delsing, Propagating phonons coupled to an artificial atom, Science **346**, 207 (2014).

[9] W. D. Oliver, Y. Yu, J. C. Lee, K. K. Berggren, L. S. Levitov, and T. P. Orlando, Mach-Zehnder interferometry in a strongly driven superconducting qubit, Science **310**, 1653 (2005).

[10] W. D. Oliver and S. O. Valenzuela, Large-amplitude driving of a superconducting artificial atom: Interferometry, cooling, and amplitude spectroscopy, Quantum Inf. Process. **8**, 261 (2009).

[11] P. Wen, A. Kockum, H. Ian, J. Chen, F. Nori, and I.-C. Hoi, Reflective amplification without population inversion from a strongly driven superconducting qubit, Phys. Rev. Lett. **120**, 063603 (2018).

[12] S. Ashhab and F. Nori, Qubit-oscillator systems in the ultrastrong-coupling regime and their potential for preparing nonclassical states, Phys. Rev. A **81**, 042311 (2010).

[13] X. Hu, Y.-x. Liu, and F. Nori, Strong coupling of a spin qubit to a superconducting stripline cavity, Phys. Rev. B

86, 035314 (2012).

[14] J. Flick, N. Rivera, and P. Narang, Strong light-matter coupling in quantum chemistry and quantum photonics, Nanophotonics **7**, 1479 (2018).

[15] D. S. Dovzhenko, S. V. Ryabchuk, Y. P. Rakovich, and I. R. Nabiev, Light–matter interaction in the strong coupling regime: configurations, conditions, and applications, Nanoscale **10**, 3589 (2018).

[16] A. Frisk Kockum, A. Miranowicz, S. De Liberato, S. Savasta, and F. Nori, Ultrastrong coupling between light and matter, Nat. Rev. Phys. **1**, 19 (2019).

[17] P. Forn-Díaz, L. Lamata, E. Rico, J. Kono, and E. Solano, Ultrastrong coupling regimes of light-matter interaction, Rev. Mod. Phys. **91**, 025005 (2019).

[18] A. Mercurio, V. Macrì, C. Gustin, S. Hughes, S. Savasta, and F. Nori, Regimes of cavity QED under incoherent excitation: From weak to deep strong coupling, Phys. Rev. Research **4**, 023048 (2022).

[19] I. Björkman, M. Kuzmanović, and G. S. Paraoanu, Observation of the two-photon Landau-Zener-Stückelberg-Majorana effect, Phys. Rev. Lett. **134**, 060602 (2025).

[20] S.-S. Gu, S. Kohler, Y.-Q. Xu, R. Wu, S.-L. Jiang, S.-K. Ye, T. Lin, B.-C. Wang, H.-O. Li, G. Cao, and G.-P. Guo, Probing two driven double quantum dots strongly coupled to a cavity, Phys. Rev. Lett. **130**, 233602 (2023).

[21] M. Sillanpää, T. Lehtinen, A. Paila, Y. Makhlin, and P. Hakonen, Continuous-time monitoring of Landau-Zener interference in a Cooper-pair box, Phys. Rev. Lett. **96**, 187002 (2006).

[22] S. Ashhab, J. R. Johansson, A. M. Zagoskin, and F. Nori, Two-level systems driven by large-amplitude fields, Phys. Rev. A **75**, 063414 (2007).

[23] J. Q. You, X. Hu, S. Ashhab, and F. Nori, Low-decoherence flux qubit, Phys. Rev. B **75**, 140515 (2007).

[24] S. N. Shevchenko, S. Ashhab, and F. Nori, Landau–Zener–Stückelberg interferometry, Phys. Rep. **492**, 1 (2010).

[25] S. N. Shevchenko, S. Ashhab, and F. Nori, Inverse Landau-Zener-Stückelberg problem for qubit-resonator systems, Phys. Rev. B **85**, 094502 (2012).

[26] M. P. Silveri, J. A. Tuorila, E. V. Thuneberg, and G. S. Paraoanu, Quantum systems under frequency modulation, Rep. Progr. Phys. **80**, 056002 (2017).

[27] O. V. Ivakhnenko, S. N. Shevchenko, and F. Nori, Nonadiabatic Landau–Zener–Stückelberg–Majorana transitions, dynamics, and interference, Phys. Rep. **995**, 1 (2023).

[28] A. I. Ryzhov, O. V. Ivakhnenko, S. N. Shevchenko, M. F. Gonzalez-Zalba, and F. Nori, Alternative fast quantum logic gates using nonadiabatic Landau-Zener-Stückelberg-Majorana transitions, Phys. Rev. Research **6**, 033340 (2024).

[29] F. Kivelä, S. Dogra, and G. S. Paraoanu, Quantum simulation of the pseudo-Hermitian Landau-Zener-Stückelberg-Majorana effect, Phys. Rev. Research **6**, 023246 (2024).

[30] S. D. Tedo, O. Feulefack, J. Danga, S. Mkam Tchouobiap, R. Keumo Tsiaze, A. Fotue, M. Hounkonnou, and L. Fai, Harmonic driving and dynamic transitions in the Landau–Zener–Stückelberg–Majorana interferometry induced by tunneling flux-driven symmetric transmon qubits, Review in Physics **13**, 100118 (2025).

[31] L. Peyruchat, F. Minganti, M. Scigliuzzo, F. Ferrari, V. Jouanny, F. Nori, V. Savona, and P. Scarlino, Landau–Zener without a qubit: multiphoton sidebands interaction and signatures of dissipative quantum chaos, npj Quantum Information **11**, 62 (2025).

[32] S. Hu, S. Li, M. Hu, and Z. Lei, Symmetry-protected Landau-Zener-Stückelberg-Majorana interference and nonadiabatic topological transport of edge states, Phys. Rev. A **111**, 052414 (2025).

[33] J. P. Pekola, P. Solinas, A. Shnirman, and D. V. Averin, Calorimetric measurement of work in a quantum system, New J. Phys. **15**, 115006 (2013).

[34] F. Yan, S. Gustavsson, A. Kamal, J. Birenbaum, A. P. Sears, D. Hover, T. J. Gudmundsen, D. Rosenberg, G. Samach, S. Weber, J. L. Yoder, T. P. Orlando, J. Clarke, A. J. Kerman, and W. D. Oliver, The flux qubit revisited to enhance coherence and reproducibility, Nat. Commun. **7**, 12964 (2016).

[35] G. Thomas and J. P. Pekola, Dynamical phase and quantum heat at fractional frequencies, Phys. Rev. Res. **5**, L022036 (2023).

[36] P. Zhelnin, L. Johns, and C. A. Argüelles, Qubit thermodynamics: Entropy production from nonadiabatic driving, ArXiv (2025), arXiv:2506.16570.

[37] B. Karimi and J. P. Pekola, Otto refrigerator based on a superconducting qubit: Classical and quantum performance, Phys. Rev. B **94**, 184503 (2016).

[38] C. Elouard, G. Thomas, O. Maillet, J. P. Pekola, and A. N. Jordan, Quantifying the quantum heat contribution from a driven superconducting circuit, Phys. Rev. E **102**, 030102 (2020).

[39] K. Ono, S. Shevchenko, T. Mori, S. Moriyama, and F. Nori, Analog of a quantum heat engine using a single-spin qubit, Phys. Rev. Lett. **125**, 166802 (2020).

[40] A. Guthrie, C. D. Satrya, Y.-C. Chang, P. Menczel, F. Nori, and J. P. Pekola, Cooper-pair box coupled to two resonators: An architecture for a quantum refrigerator, Phys. Rev. Appl. **17**, 064022 (2022).

[41] T. Uusnäkki, T. Mörstedt, W. Teixeira, M. Rasola, and M. Möttönen, Experimental realization of a quantum heat engine based on dissipation-engineered superconducting circuits (2025), arXiv:2502.20143 [quant-ph].

[42] R. Upadhyay, G. Thomas, Y.-C. Chang, D. S. Golubev, A. Guthrie, A. Gubaydullin, J. T. Peltonen, and J. P. Pekola, Robust strong-coupling architecture in circuit quantum electrodynamics, Phys. Rev. Appl. **16**, 044045 (2021).

[43] A. N. Omelyanchouk, S. N. Shevchenko, Y. S. Greenberg, O. Astafiev, and E. Il'ichev, Quantum behavior of a flux qubit coupled to a resonator, Low. Temp. Phys. **36**, 893 (2010).

[44] S. Ashhab, T. Fuse, F. Yoshihara, S. Kim, and K. Semba, Controlling qubit-oscillator systems using linear parameter sweeps, New J. Phys. **25**, 093011 (2023).

[45] J. Johansson, P. Nation, and F. Nori, QuTiP: An open-source Python framework for the dynamics of open quantum systems, Comput. Phys. Commun. **183**, 1760 (2012).

[46] J. R. Johansson, P. D. Nation, and F. Nori, QuTiP 2: A Python framework for the dynamics of open quantum systems, Comput. Phys. Commun. **184**, 1234 (2013).

[47] N. Lambert, E. Giguère, P. Menczel, B. Li, P. Hopf, G. Suárez, M. Gali, J. Lishman, R. Gadhvi, R. Agarwal, A. Galicia, N. Shammah, P. Nation, J. R. Johansson, S. Ahmed, S. Cross, A. Pitchford, and F. Nori, QuTiP 5: The Quantum Toolbox in Python (2024).

[48] T. Suzuki, H. Nakazato, R. Grimaudo, and A. Messina, Analytic estimation of transition between instantaneous eigenstates of quantum two-level system, Sci. Rep. **8**, 17433 (2018).

[49] S. N. Shevchenko, G. Oelsner, Y. S. Greenberg, P. Macha, D. S. Karpov, M. Grajcar, U. Hübner, A. N. Omelyanchouk, and E. Il'ichev, Amplification and attenuation of a probe signal by doubly dressed states, Phys. Rev. B **89**, 184504 (2014).

[50] P. Y. Wen, O. V. Ivakhnenko, M. A. Nakonechnyi, B. Suri, J.-J. Lin, W.-J. Lin, J. C. Chen, S. N. Shevchenko, F. Nori, and I.-C. Hoi, Landau-Zener-Stückelberg-Majorana interferometry of a superconducting qubit in front of a mirror, Phys. Rev. B **102**, 075448 (2020).

[51] F.-E. von Horstig, L. Peri, S. Barraud, S. N. Shevchenko, C. J. B. Ford, and M. F. Gonzalez-Zalba, Floquet interferometry of a dressed semiconductor quantum dot, ArXiv , 2407.14241 (2024).

[52] A. M. Satanin, M. V. Denisenko, S. Ashhab, and F. Nori, Amplitude spectroscopy of two coupled qubits, Phys. Rev. B **85**, 184524 (2012).